processes

MDPI

Article

Numerical Study of the Buckling Response of Stiffened FG Graphene-Reinforced Multilayer Composite Cylindrical Panels

Zhihong Liu [1,*], Francesco Tornabene [2,*], Rossana Dimitri [2] and Masoud Babaei [3]

[1] School of Statistics and Big Data, Zhengzhou College of Finance and Economics, Zhengzhou 450044, China
[2] Department of Innovation Engineering, University of Salento, 73100 Lecce, Italy; rossana.dimitri@unisalento.it
[3] Department of Mechanical Engineering, University of Eyvanekey, Eyvanekey 99888-35918, Iran; masoudbabaei@eyc.ac.ir
[*] Correspondence: zhihongliu888@163.com (Z.L.); francesco.tornabene@unisalento.it (F.T.)

Abstract: The present research aims at determining the axial buckling load of stiffened multilayer cylindrical shell panels made of functionally graded graphene-reinforced composites (FG-GPL RCs). Rings and stringers are applied as stiffening tools for shell panels, whose elastic properties are determined according to the Halpin–Tsai relations. The virtual work principle and finite element approach are implemented here, according to a first-order shear deformation theory (FSDT) and Lekhnitskii smeared stiffener approach, in order to determine the governing equations of the stability problem. Four different dispersions of nanofillers are assumed in the thickness direction, including the FG-X, FG-A, FG-O, and UD distributions. A large systematic investigation considers the effect of different geometric and material parameters on the buckling loads and mode shapes of the stiffened FG-GPL RC cylindrical shell panel, primarily the dispersion and weight fractions of the nanofiller, the number of rings and stringers, and the boundary conditions, with useful insights for design purposes.

Keywords: axial buckling; FEM; FSDT; functionally graded material; graphene-reinforced composite multilayer cylindrical panel

check for updates

Citation: Liu, Z.; Tornabene, F.; Dimitri, R.; Babaei, M. Numerical Study of the Buckling Response of Stiffened FG Graphene-Reinforced Multilayer Composite Cylindrical Panels. *Processes* **2024**, *12*, 430. https://doi.org/10.3390/pr12030430

Academic Editors: Zhou Li and Raul D. S. G. Campilho

Received: 9 October 2023
Revised: 17 January 2024
Accepted: 18 February 2024
Published: 20 February 2024

1. Introduction

In the last decades, a great effort by scientists has been devoted to increase the mechanical performances and durability of many structural members, primarily resorting to polymeric or metal nanocomposite materials, where nanoparticles can be dispersed within a polymeric or metallic matrix, with different distributions, in line with design requirements. The uniform dispersion of nanoparticles as reinforcement phase is desirable, even though their high level of energy can cause some agglomeration phenomena, with low nanoparticle weight fractions. In addition, there are some practical procedures, such as the use of an ultrasonic bath instead of traditional mixing, to ensure the uniform dispersion of nanoparticles in the matrix. Another way to enhance the mechanical performance of a structure stems from the application of ribs and stringers as strengthening members. In addition, the connection type between stiffeners and original structure plays a key role in the final strength of the assembled configuration, due to the presence of stress concentrations near to the connection points. Such connections can include glue, welding, screws, or rivets that can significantly affect the overall response of the stiffened structure.

There are a lot of works in the literature that have focused on different strengthening strategies for the improvement of the mechanical performances of structures under different loading conditions, both in a static and dynamic sense. Among GPL-reinforced applications, Mollaei et al. [1] applied the 3D finite element elasticity solution and virtual work principle to assess the buckling response of FG-GPL RC cylindrical shell panels under a torsional load. Kiani [2], instead, employed a generalized differential quadrature method (GDQM) and an equilibrium criterion to determine the buckling load of FG-GPL conical shells under a thermo-mechanical loading condition, accounting for a FSDT for shell structures.

Lei et al. [3] used a Ritz approach to estimate the buckling load of FG-GPL RC laminated plates in thermal conditions applying the FSDT. Shahgholian et al. [4,5] also applied the Hamiltonian principle, FSDT basics, and Rayleigh–Ritz approach to evaluate the buckling [4] and torsional buckling [5] loads of FG porous hollow cylinders reinforced by GPLs. The same FSDT theoretical basics were also applied by Dong et al. [6] to analytically evaluate the buckling load of FG cylinders with porosities and reinforced by GPLs. The same Ritz approach was also employed by Chen et al. [7] in order to control the vibration and the geometrically nonlinear buckling behavior of FG-GPL nanocomposite porous beams. In another work [8], the same authors applied the Ritz approach to determine the elastic buckling and natural frequency response of composite beams reinforced by GPLs, including FG porosities. Zhang et al. [9] presented an analytical solution for the thermo-mechanical analysis of porous FG graphene-reinforced cylindrical panels using an improved third-order shear deformation theory. Sobhani et al. [10], instead, analyzed the natural frequencies of hybrid porous nanocomposite-joined hemispherical–cylindrical–conical shells based on a FSDT and GDQM procedure. At the same time, Yang et al. [11] combined the FSDT and the Chebyshev–Ritz approach to perform a comprehensive investigation of the buckling response for porous FG-GPL nanocomposite rectangular plates, whereas Zhou et al. [12] evaluated the buckling load of FG porous cylinders reinforced with GPLs, based on a classical theory of shells and higher-order shear deformation theory (HSDT). A novel numerical model was introduced by Ansari et al. [13] to estimate the buckling load of porous FG-GPL plate-type structures, whose governing measures were determined based on the Hamiltonian principle and HSDT. Similarly, Yaghoobi and Taheri [14] proposed an analytical procedure to study the buckling behavior of sandwiched rectangular plates with a FG porous core reinforced with GPLs, whereas Tao and Dai [15] applied the isogeometric approach to accurately study the post-buckling behavior of cylindrical shell panels with a FG porous core reinforced by GPL nanofillers. This last computational strategy was also proposed by Nguyen et al. [16] to determine the buckling load and natural frequency of FG-GPL porous rectangular plates according to HSDTs.

For further applications of the HSDT and finite element approach for the buckling and post-buckling behavior of different shells and panels, the reader is referred to Refs. [17–23], whose limit cases can be represented by curved beams [24–26], as well as by a classical shell theory, or thin-walled shell theory as proposed in [27,28], respectively, for shell structures with stiffeners. For these last structural cases, we briefly recall some relevant works from the recent literature focusing on the influence of stiffeners such as ribs and stringers on the buckling response of shell members. For example, Shahani and Kiarasi [29] numerically and experimentally investigated the buckling load of stiffened cylindrical shells with cut outs under a uniform axial loading. Similarly, Wu et al. [30] focused on the buckling response of composite stiffened panels under an impact force, and Tran et al. [31] numerically computed the buckling force of stiffened curved panels under an axial force. A classical finite element approach was followed by Grondin et al. [32] to investigate the buckling response of stiffened steel rectangular plates, whereas Reddy et al. [33] proposed a layerwise theory for the buckling study of stiffened hollow cylinders. An interesting review paper about the stability response of isotropic and composite stiffened panels can be found in Ref. [34], whereas some optimization procedures are proposed in Refs. [35–39] to improve the mechanical response of shell structures with different shapes in the presence of stiffeners. One of the most common computational tools to treat similar problems relies on the classical finite element method (FEM), as implemented by Ifayefunmi and Ruhan [40] to evaluate the buckling response of stiffened joined conical–cylindrical shell-type structures under an axial force, but also to model the buckling of grid-stiffened composite conical shells and stiffened shell panel structures [41,42].

Despite the large use of classical FEM, there are few works theoretically defining the buckling load based on a Lekhnitskii smeared technique, where the connection between the original structure and stiffeners is considered ideal in absence of rivets, screws, and welding. For example, Duc and Thang [43] considered the nonlinear buckling response of imperfect cylindrical shells with stiffeners made of FG materials (FGMs) in thermal conditions. In another investigation [44], the same authors proposed a nonlinear analysis of stiffened FGM cylinders resting on an elastic medium and subjected to an axial force. Similarly, Duc [45] studied the nonlinear vibration response of imperfect FGM doubly curved panels with stiffeners resting on an elastic medium. Duc and Cong [46] applied the classical shell theory together with the Galerkin approach to study the nonlinear thermal response of stiffened conical shells made of FGMs on an elastic substrate.

Based on the literature overview, it has been clearly shown that nanoparticle-based reinforcements as well as the application of orthogonal stiffeners such as rings and stringers can singly provide a great effect on the buckling response of shell structures. However, the combined effect of both aspects has been not investigated yet, as proposed in the present work for the buckling study of stiffened FG graphene-reinforced composite multilayer cylindrical shell panels. In such a context, four different distributions of GPL reinforcements are assumed here throughout the thickness direction of the cylindrical panels, whereas a Lekhnitskii smeared technique is considered to model the connection between FG-GPL shell panels and stiffeners. Moreover, the Halpin–Tsai relations are established here to estimate the equivalent mechanical properties of the shell panel. The FSDT, together with the principle of virtual work and finite element procedure, are also adopted to determine the governing equations of the problem. A systematic investigation is performed to check for the effect of several parameters, including the weight fractions and patterns of GPLs, different boundary conditions, geometries, and numbers of stiffeners, on the buckling response of stiffened FG-GPL cylindrical shell panels. The work is organized as follows. After this brief introduction, we provide the main basic principles of the theoretical model in Section 2, starting with the geometrical and mechanical definition of the selected problem. The governing equations of the problem are then solved numerically according to a finite element approximation, as proposed in Section 3, from a theoretical perspective, and they are applied numerically in Section 4 within a large parametric investigation. The main concluding remarks can be found in Section 5, with useful suggestions from both a theoretical and a design standpoint for different engineering applications of novel composite structural members optimized by simply tuning the FG graphene reinforcement phase.

2. Theoretical Formulation

2.1. Geometrical and Mechanical Properties

Let us consider a stiffened FG-GPL multilayer cylindrical shell panel under a compressive axial force (Figure 1), with length L, span angle β, radius R, and thickness h. As visible in the same figure, let us assume the (x, θ, z) system of coordinates, accounting for the axial, hoop, and radial axes, respectively. We account for a shell panel stiffened with longitudinal stiffeners (stringers) and circumferential stiffeners (rings), reinforced by different GPL patterns, as reported in Figure 1.

GPLs can be distributed in the polymer matrix uniformly or non-uniformly. In the last case, the weight fraction of the nanofiller (GPL) is functionally graded across the radial direction of the shell panel, which is made of n_L layers. More in detail, we consider four different volume fraction distributions of FG GPL-RCs, namely, a uniform pattern (UD) in addition to FG-A, O, and X patterns. In the uniform case, the GPL weight fraction remains constant for each layer, yielding to a homogeneous isotropic GPL-RC structure. For FG patterns, instead, the weight fraction of GPLs varies linearly across the thickness of the panel. More in detail, for FG-X distributions, the weight fraction of GPLs assumes the maximum value at the inner and outer layers, whereas for a FG-O distribution, the weight fraction obtains the maximum value at the mid-layers. Moreover, for an A-GPLRC-type distribution, the weight fraction is maximum at the inner layer and decreases continuously for an increased distance from it, assuming the lowest quantity of GPLs at the external surface of the shell. For different GPL distributions, the equivalent weight fraction can be evaluated as [47–51].

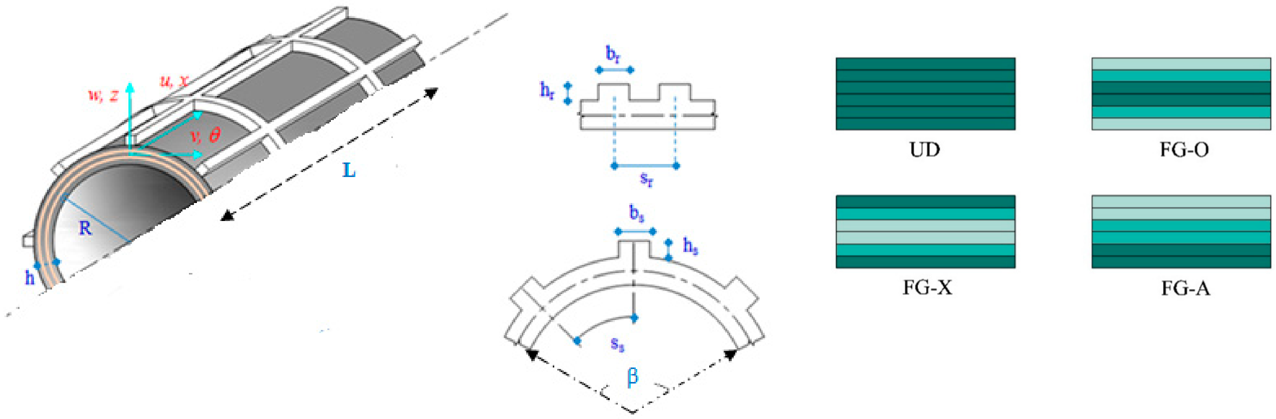

Figure 1. Geometrical scheme of a stiffened FG-GPL multilayer shell panel with four different distributions of GPLs.

$$\begin{cases} UD: \ V_{GPL}^{(k)} = V_{GPL}^{*} \\ FG-X: \ V_{GPL}^{(k)} = 2V_{GPL}^{*}\frac{|2k-n_L-1|}{n_L} \\ FG-O: \ V_{GPL}^{(k)} = 2V_{GPL}^{*}\left(1-\frac{|2k-n_L-1|}{n_L}\right) \\ FG-\Lambda: \ V_{GPL}^{(k)} = V_{GPL}^{*}\left(\frac{2(n_L-k+1)-1}{n_L}\right) \end{cases} \tag{1}$$

Here, $V_{GPL}^{(k)}$ refers to the volume content of GPL in each layer of the panel, with k varying from 1 to n_L; V_{GPL}^{*} stands for the volume fraction of nanofillers, which can be evaluated as follows:

$$V_{GPL}^{*} = \frac{\Delta_{GPL}\rho_m}{\Delta_{GPL}\rho_m + \rho_{GPL} - \Delta_{GPL}\rho_{GPL}} \tag{2}$$

where Δ_{GPL} is the weight fraction of the nanofillers, and ρ_{GPL} and ρ_m stand for the mass density of the nanofillers and polymeric matrix, respectively.

According to Halpin–Tsai micromechanics [44–48], the elasticity modulus of the panel can be described as

$$E = \frac{3}{8}\left(\frac{1+\varepsilon_L^{GPL}\eta_L^{GPL}V_{GPL}}{1-\eta_L^{GPL}V_{GPL}}\right)E_m + \frac{5}{8}\left(\frac{1+\varepsilon_W^{GPL}\eta_W^{GPL}V_{GPL}}{1-\eta_W^{GPL}V_{GPL}}\right)E_{GPL} \tag{3}$$

$$\varepsilon_L^{GPL} = \frac{2l_{GPL}}{t_{GPL}} \tag{4}$$

$$\varepsilon_W^{GPL} = \frac{2w_{GPL}}{t_{GPL}} \tag{5}$$

$$\eta_L^{GPL} = \frac{E_{GPL}-E_m}{E_{GPL}+\varepsilon_L^{GPL}E_m} \tag{6}$$

$$\eta_W^{GPL} = \frac{E_{GPL}-E_m}{E_{GPL}+\varepsilon_W^{GPL}E_m} \tag{7}$$

where E_m and E_{GPL} stand for the elasticity modulus for the matrix and nanofillers, respectively. In addition, l_{GPL}, w_{GPL}, t_{GPL}, and V_{GPL} refer to the length, width, thickness, and volume fraction of the nanofillers, respectively. The rule of mixture is also employed to evaluate the Poisson's ratio and mass density of the GPL-RC:

$$\rho = \rho_{GPL}V_{GPL} + \rho_m(1-V_{GPL}) \tag{8}$$

$$v = v_{GPL}V_{GPL} + v_m(1-V_{GPL}) \tag{9}$$

where ν_{GPL} and ν_m refer to the Poisson's ratio of the nanofillers and matrix, respectively. Thus, the shear modulus G of the shell is determined as

$$G = \frac{E}{2(1+\nu)} \tag{10}$$

2.2. Mathematical Problem

A FSDT is considered here to describe the displacement field, and a Lekhnitskii smeared stiffeners assumption is employed to define the relation between the main structure and its rings and stringers. Applying the FSDT of shells, the displacement components of the shell are defined as

$$\begin{aligned} u(x,\theta,z,t) &= u_0(x,\theta,t) + z\,\phi_x(x,\theta,t) \\ v(x,\theta,z,t) &= v_0(x,\theta,t) + z\,\phi_\theta(x,\theta,t) \\ w(x,\theta,z,t) &= w_0(x,\theta,t) \end{aligned} \tag{11}$$

where u_0, v_0, w_0 are the kinematic components of the mid-plane of the panel along the axial, circumferential, and radial directions, respectively. Also, $\phi_x(x,\theta,t)$, $\phi_\theta(x,\theta,t)$ are the rotations of the mid-plane around the x and θ axes, respectively. The kinematic relations are also defined as

$$\begin{aligned} \varepsilon_x &= \varepsilon_x^0 + z\,k_x \\ \varepsilon_\theta &= \varepsilon_\theta^0 + z\,k_\theta \\ \gamma_{x\theta} &= \gamma_{x\theta}^0 + z\,k_{x\theta} \\ \gamma_{\theta z} &= \gamma_{\theta z}^0 \\ \gamma_{xz} &= \gamma_{xz}^0 \end{aligned} \tag{12}$$

where

$$\begin{array}{lll} \varepsilon_x^0 = \frac{\partial u_0}{\partial x}; & k_x = \frac{\partial \phi_x}{\partial x}; & \varepsilon_\theta^0 = \frac{\partial v_0}{R\partial\theta} + \frac{w_\circ}{R}; \\ k_\theta = \frac{\partial \phi_\theta}{R\partial\theta}; & \gamma_{x\theta}^0 = \frac{\partial u_\circ}{R\partial\theta} + \frac{\partial v_\circ}{\partial x}; & k_{x\theta} = \frac{\partial \phi_x}{R\partial\theta} + \frac{\partial \phi_\theta}{\partial x}; \\ \gamma_{\theta z} = \phi_\theta + \frac{\partial w_\circ}{R\partial\theta} - \frac{v_\circ}{R}; & \gamma_{xz}^0 = \phi_x + \frac{\partial w_\circ}{\partial x}; & \end{array} \tag{13}$$

Based on the Lekhnitskii approach, the resultants of forces and moments are defined as [52]

$$\begin{aligned} N_x &= (A_{11} + \tfrac{E_s A_s}{s_s})\varepsilon_x^0 + A_{12}\varepsilon_\theta^0 + (B_{11} + \tfrac{E_s A_s z_s}{s_s})k_x + B_{12}k_\theta \\ N_\theta &= A_{12}\varepsilon_x^0 + (A_{22} + \tfrac{E_r A_r}{s_r})\varepsilon_\theta^0 + B_{12}k_x + (B_{22} + \tfrac{E_r A_r z_r}{s_r})k_\theta \\ N_{x\theta} &= A_{66}\gamma_{x\theta}^0 + B_{66}k_{x\theta} \\ M_x &= (B_{11} + \tfrac{E_s A_s z_s}{s_s})\varepsilon_x^0 + B_{12}\varepsilon_\theta^0 + (D_{11} + \tfrac{E_s I_s}{s_s})k_x + D_{12}k_\theta \\ M_\theta &= B_{12}\varepsilon_x^0 + (B_{22} + \tfrac{E_r A_r z_r}{s_r})\varepsilon_\theta^0 + D_{12}k_x + (D_{22} + \tfrac{E_r I_r}{s_r})k_\theta \\ M_{x\theta} &= B_{66}\gamma_{x\theta}^0 + D_{66}k_{x\theta} \\ &\begin{cases} Q_\theta = k_s(A_{44} + \tfrac{G_r A_r}{s_r})\gamma_{\theta z} \\ Q_x = k_s(A_{55} + \tfrac{G_s A_s}{s_s})\gamma_{xz} \end{cases} \end{aligned} \tag{14}$$

with

$$\begin{array}{lll} A_{11} = A_{22} = \int\limits_{-\frac{h}{2}}^{\frac{h}{2}} \frac{E}{1-v^2}dz; & B_{11} = B_{22} = \int\limits_{-\frac{h}{2}}^{\frac{h}{2}} \frac{E}{1-v^2}zdz; & D_{11} = D_{22} = \int\limits_{-\frac{h}{2}}^{\frac{h}{2}} \frac{E}{1-v^2}z^2dz; \\ A_{12} = \int\limits_{-\frac{h}{2}}^{\frac{h}{2}} \frac{vE}{1-v^2}dz; & B_{12} = \int\limits_{-\frac{h}{2}}^{\frac{h}{2}} \frac{vE}{1-v^2}zdz; & D_{12} = \int\limits_{-\frac{h}{2}}^{\frac{h}{2}} \frac{vE}{1-v^2}z^2dz; \\ A_{66} = \int\limits_{-\frac{h}{2}}^{\frac{h}{2}} \frac{E}{2[1+v]}dz; & B_{66} = \int\limits_{-\frac{h}{2}}^{\frac{h}{2}} \frac{E}{2[1+v]}zdz; & D_{66} = \int\limits_{-\frac{h}{2}}^{\frac{h}{2}} \frac{E}{2[1+v]}z^2dz; \\ A_{44} = A_{55} = \int\limits_{-\frac{h}{2}}^{\frac{h}{2}} \frac{E}{2[1+v]}dz; & & \end{array} \tag{15}$$

$$I_s = \frac{b_s h_s^3}{12} + A_s z_s^2; \quad I_r = \frac{b_r h_r^3}{12} + A_r z_r^2; \quad z_s = \pm\frac{h_s + h}{2}; \quad z_r = \pm\frac{h_r + h}{2}$$

The normal and tangential elasticity moduli of stringers and rings are defined as E_s, G_s and E_r, G_r, respectively, while assuming a shear correction factor $k_s = 5/6$. Both ribs and stringers as well as the main panel are considered to be perfectly joined, and each part is made of the same material. A uniaxial stress state is also assumed for both rings and stringers, which are defined geometrically by height $h_r,\ h_s$, and width $b_r,\ b_s$, respectively, for a global cross-section area $A_r,\ A_s$.

Moreover, the distances between two adjacent stringers and each ring are denoted by S_s and S_r, respectively, whereas the distances between the centroid of each stringer and ring from the mid-surface of the panel are labeled as z_s and z_r, respectively. The resultants of force and moment in matrix form are defined as

$$\begin{Bmatrix} N_x \\ N_\theta \\ N_{x\theta} \\ M_x \\ M_\theta \\ M_{x\theta} \end{Bmatrix} = \begin{bmatrix} \overline{A}_{11} & \overline{A}_{12} & 0 & \overline{B}_{11} & \overline{B}_{12} & 0 \\ \overline{A}_{12} & \overline{A}_{22} & 0 & \overline{B}_{12} & \overline{B}_{22} & 0 \\ 0 & 0 & \overline{A}_{66} & 0 & 0 & \overline{B}_{66} \\ \overline{B}_{11} & \overline{B}_{12} & 0 & \overline{D}_{11} & \overline{D}_{12} & 0 \\ \overline{B}_{12} & \overline{B}_{22} & 0 & \overline{D}_{12} & \overline{D}_{22} & 0 \\ 0 & 0 & \overline{B}_{66} & 0 & 0 & \overline{D}_{66} \end{bmatrix} \begin{Bmatrix} \varepsilon_x^0 \\ \varepsilon_\theta^0 \\ \gamma_{x\theta}^0 \\ k_x \\ k_\theta \\ k_{x\theta} \end{Bmatrix}, \tag{16}$$
$$\begin{Bmatrix} Q_\theta \\ Q_x \end{Bmatrix} = k_s \begin{bmatrix} \overline{A}_{44} & 0 \\ 0 & \overline{A}_{55} \end{bmatrix} \begin{Bmatrix} \gamma_{\theta z} \\ \gamma_{xz} \end{Bmatrix}$$

with

$$\overline{A} = \begin{bmatrix} \overline{A}_{11} & \overline{A}_{12} & 0 \\ \overline{A}_{12} & \overline{A}_{22} & 0 \\ 0 & 0 & \overline{A}_{66} \end{bmatrix},$$
$$\overline{B} = \begin{bmatrix} \overline{B}_{11} & \overline{B}_{12} & 0 \\ \overline{B}_{12} & \overline{B}_{22} & 0 \\ 0 & 0 & \overline{B}_{66} \end{bmatrix},$$
$$\overline{D} = \begin{bmatrix} \overline{D}_{11} & \overline{D}_{12} & 0 \\ \overline{D}_{12} & \overline{D}_{22} & 0 \\ 0 & 0 & \overline{D}_{66} \end{bmatrix}, \quad \overline{E} = k_s \begin{bmatrix} \overline{A}_{44} & 0 \\ 0 & \overline{A}_{55} \end{bmatrix}$$

$$\begin{array}{llll} \overline{A}_{11} = A_{11} + \frac{E_s A_s}{s_s}; & \overline{A}_{12} = A_{12}; & \overline{A}_{22} = A_{22} + \frac{E_r A_r}{s_r}; & \overline{A}_{66} = A_{66}; \\ \overline{A}_{44} = A_{44} + \frac{G_r A_r}{s_r}; & \overline{A}_{55} = A_{55} + \frac{G_s A_s}{s_s}; & & \\ \overline{B}_{11} = B_{11} + \frac{E_s A_s z_s}{s_s}; & \overline{B}_{12} = B_{12}; & & \\ \overline{B}_{22} = B_{22} + \frac{E_r A_r z_r}{s_r}; & \overline{B}_{66} = B_{66} & & \\ \overline{D}_{11} = D_{11} + \frac{E_s I_s}{s_s}; & \overline{D}_{12} = D_{12}; & & \\ \overline{D}_{22} = D_{22} + \frac{E_r I_r}{s_r}; & \overline{D}_{66} = D_{66} & & \end{array}$$

The principle of virtual work is now applied to determine the governing equations of the problem:

$$\begin{aligned} &\delta U - \delta W = 0 \\ &U = \frac{1}{2}\int_s \left[N_x \varepsilon_x^0 + N_\theta \varepsilon_\theta^0 + N_{x\theta}\gamma_{x\theta}^0 + M_x k_x + M_\theta k_\theta + M_{x\theta} k_{x\theta} + Q_\theta \gamma_{\theta z} + Q_x \gamma_{xz}\right] R d\theta dx, \\ &W = \frac{1}{2}\int_s \left[P_x \left(\frac{\partial w_0}{\partial x}\right)^2\right] R d\theta dx \end{aligned} \tag{17}$$

with U the strain energy, and W the external work associated with a uniform compressive axial load applied on the bases of the shell. A homogenous isotropic material is assumed for all stiffeners, such that $E_s = E_r = E_m$.

Hence, the strain energy for the stiffened structure is defined as

$$U = \iint \begin{Bmatrix} N_x \varepsilon_x^0 + N_\theta\ \varepsilon_\theta^0 + N_{x\theta}\gamma_{x\theta}^0 + M_x K_x + M_\theta K_\theta + \\ M_{x\theta} K_{x\theta} + Q_x \gamma_{xz} + Q_\theta \gamma_{\theta z} \end{Bmatrix} R\ dx\ d\theta \tag{18}$$

which can be arranged in the following matrix form:

$$U = \left([N_x, N_\theta, N_{X\theta}] \begin{bmatrix} \varepsilon^0{}_x \\ \varepsilon^0{}_\theta \\ \gamma^0{}_{x\theta} \end{bmatrix} + [M_x, M_\theta, M_{X\theta}] \begin{bmatrix} K_x \\ K_\theta \\ K_{x\theta} \end{bmatrix} + [Q_x\, Q_\vartheta] \begin{bmatrix} \gamma_{XZ} \\ \gamma_{\theta Z} \end{bmatrix} \right) R dx d\theta \tag{19}$$

Also, the kinematic relations (12) and (13) can be defined in the following matrix form:

$$\begin{gathered}
\begin{bmatrix} \varepsilon_x \\ \varepsilon_\theta \\ \gamma_{x\theta} \end{bmatrix} = \begin{bmatrix} \varepsilon^0{}_x \\ \varepsilon^0{}_\theta \\ \gamma^0{}_{x\theta} \end{bmatrix} + Z \\
\begin{bmatrix} K_x \\ K_\theta \\ K_{x\theta} \end{bmatrix} = \begin{bmatrix} \frac{\partial}{\partial x} & 0 & 0 & Z\frac{\partial}{\partial x} & 0 \\ 0 & \frac{1}{R}\frac{\partial}{\partial \theta} & \frac{1}{R} & 0 & Z\frac{1}{R}\frac{\partial}{\partial \theta} \\ \frac{1}{R}\frac{\partial}{\partial \theta} & \frac{\partial}{\partial x} & 0 & Z\frac{1}{R}\frac{\partial}{\partial \theta} & Z\frac{\partial}{\partial x} \end{bmatrix} \begin{bmatrix} U_0 \\ V_0 \\ W_0 \\ \varphi_X \\ \varphi_\theta \end{bmatrix} = d_1 Q \\
\begin{bmatrix} \gamma^0{}_{xz} \\ \gamma^0{}_{\theta z} \end{bmatrix} = \begin{bmatrix} 0 & 0 & \frac{\partial}{\partial x} & 1 & 0 \\ 0 & \frac{-1}{R} & \frac{1}{R}\frac{\partial}{\partial \theta} & 0 & 1 \end{bmatrix} \begin{bmatrix} U_0 \\ V_0 \\ W_0 \\ \varphi_X \\ \varphi_\theta \end{bmatrix} = d_2 Q, \\
\begin{bmatrix} \varepsilon^0{}_x \\ \varepsilon^0{}_\theta \\ \gamma^0{}_{x\theta} \end{bmatrix} = \begin{bmatrix} \frac{\partial}{\partial x} & 0 & 0 & 0 & 0 \\ 0 & \frac{1}{R}\frac{\partial}{\partial \theta} & \frac{1}{R} & 0 & 0 \\ \frac{1}{R}\frac{\partial}{\partial \theta} & \frac{\partial}{\partial x} & 0 & 0 & 0 \end{bmatrix} \begin{bmatrix} U_0 \\ V_0 \\ W_0 \\ \varphi_X \\ \varphi_\theta \end{bmatrix} = d_3 Q \\
\begin{bmatrix} K_x \\ K_\theta \\ K_{x\theta} \end{bmatrix} = \begin{bmatrix} 0 & 0 & 0 & \frac{\partial}{\partial x} & 0 \\ 0 & 0 & 0 & 0 & \frac{1}{R}\frac{\partial}{\partial \theta} \\ 0 & 0 & 0 & \frac{1}{R}\frac{\partial}{\partial \theta} & \frac{\partial}{\partial x} \end{bmatrix} \begin{bmatrix} U_0 \\ V_0 \\ W_0 \\ \varphi_X \\ \varphi_\theta \end{bmatrix} = d_4 Q, \\
Q = \begin{bmatrix} U_0 \\ V_0 \\ W_0 \\ \varphi_X \\ \varphi_\theta \end{bmatrix}
\end{gathered} \tag{20}$$

Hence, by substitution of Equation (20) into Equation (19), the strain energy can be defined in variational form as

$$\delta U = \int \left(\begin{array}{l} \left((d_3 Q)^T \overline{A}^{\,T} + (d_4 Q)^T \overline{B}^{\,T} \right) (d_3 \delta Q) + \\ \left((d_3 Q)^T \overline{B}^{\,T} + (d_4 Q)^T \overline{D}^{\,T} \right) (d_4 \delta Q) + (d_2 Q)^T \overline{e}^{\,T} (d_2 \delta Q) \end{array} \right) R \, dx \, d\theta \tag{21}$$

3. Finite Element Modeling

A numerical procedure based on classical finite elements is now applied to solve the governing equations of a stiffened FG-GPL multilayer cylindrical panel in a discrete manner. A two-dimensional, four-noded element with 20 degrees of freedom (DOFs) is adopted to discretize the model, where the shape functions in the x and θ axes are referred to a local-coordinate system (ξ, η) of the following type:

$$\xi = \frac{2(x - x_c)}{L^{(e)}} \quad \eta = \frac{2(\theta - \theta_c)}{\beta^{(e)}} \tag{22}$$

where $-1 \le \xi,\ \eta \le 1$ in the x and θ axes. Moreover, $L^{(e)}$ and $\beta^{(e)}$ are the length and span angle for each element, respectively. Also, θ_c and x_c are the circumferential and axial coordinates of the center for each element. The approximating functions for each element are defined in terms of natural coordinates and displacement components as follows:

$$\begin{Bmatrix} \Psi_i \\ \Psi_j \\ \Psi_k \\ \Psi_m \end{Bmatrix} = \frac{1}{4} \begin{Bmatrix} (1+\xi)(1-\eta) \\ (1+\xi)(1+\eta) \\ (1-\xi)(1+\eta) \\ (1-\xi)(1-\eta) \end{Bmatrix} \tag{23}$$

$$\left(\begin{pmatrix} \Psi_1 & \cdots & 0 \\ \vdots & \ddots & \vdots \\ 0 & \cdots & \Psi_1 \end{pmatrix} \cdots \begin{pmatrix} \Psi_4 & \cdots & 0 \\ \vdots & \ddots & \vdots \\ 0 & \cdots & \Psi_4 \end{pmatrix} \right) \begin{Bmatrix} u_{01} \\ v_{01} \\ w_{01} \\ \varphi_{x1} \\ \varphi_{\theta 1} \\ \vdots \\ u_{04} \\ v_{04} \\ w_{04} \\ \varphi_{x4} \\ \varphi_{\theta 4} \end{Bmatrix} = \psi\, q(e)$$

where $\Psi_n,\ n = 1,2,3,4$ are the shape function components, Ψ is the shape function matrix, and u_{0i}, v_{0i}, w_{0i}, φ_{xi}, and $\varphi_{\theta i}$ stand for the nodal DOFs defined as

$$\begin{aligned} &u_0 = \sum_{i=1}^{4} \Psi_i U_{0i} \quad v_0 = \sum_{i=1}^{4} \Psi_i V_{0i} \quad w_0 = \sum_{i=1}^{4} \Psi_i W_{0i} \\ &\varphi_x = \sum_{i=1}^{4} \Psi_i \theta_{xi} \quad \varphi_\theta = \sum_{i=1}^{4} \Psi_i \theta_{\theta i} \end{aligned} \tag{24}$$

By substitution of Equation (24) into Equations (17) and (21), the virtual work principle (17) can be rewritten as

$$\int_{\Omega_0^e} \left[\begin{pmatrix} (d_3\Psi)^T \overline{A}^{\,T} (d_3\Psi) + (d_4\Psi)^T \overline{B}^{\,T} (d_3\Psi) + \\ (d_3\Psi)^T \overline{B}^{\,T} (d_4\Psi) + (d_4\Psi)^T \overline{D}^{\,T} (d_4\Psi) \\ +(d_2\Psi)^T \overline{e}^{\,T} d_2 - P_x \overline{\Psi}_1^{\,T} \overline{\Psi}_1 \Psi \end{pmatrix} q^{(e)} \right] R dx d\theta = 0 \tag{25}$$

where

$$\overline{\psi}_1 = \begin{bmatrix} 0 & 0 & 0 & 0 & 0 & \ldots & 0 & 0 & 0 & 0 & 0 \\ 0 & 0 & 0 & 0 & 0 & \ldots & 0 & 0 & 0 & 0 & 0 \\ 0 & 0 & \frac{\partial \psi_1}{\partial x} & 0 & 0 & \ldots & 0 & 0 & \frac{\partial \psi_4}{\partial x} & 0 & 0 \\ 0 & 0 & 0 & 0 & 0 & \ldots & 0 & 0 & 0 & 0 & 0 \\ 0 & 0 & 0 & 0 & 0 & \ldots & 0 & 0 & 0 & 0 & 0 \end{bmatrix}_{5*20} \tag{26}$$

In addition, by replacing $d_2\Psi = B_2$, $d_3\Psi = B_3$, $d_4\Psi = B_4$ into Equation (25), the following equation is derived for a cylindrical panel element:

$$\left(k_1 + k_2 + k_3 - P_x k_g\right)^{(e)} q^{(e)} = 0 \tag{27}$$

with

$$\begin{aligned} k_1^e &= \int \left[{B_3}^T \overline{A}^{\ T} + {B_4}^T \overline{B}^{\ T} B_3 \right] R\, dx\, d\theta \\ k_2^e &= \int \left[{B_3}^T \overline{B}^{\ T} B_4 + {B_4}^T \overline{D}^{\ T} B_4 \right] R\, dx\, d\theta \\ k_3^e &= \int \left[{B_2}^T \overline{e}^{\ T} B_2 \right] R\, dx\, d\theta \\ k_g^e &= \int \overline{\Psi}_1^{\ T} \overline{\Psi}_1 R\, dx\, d\theta \end{aligned} \tag{28}$$

where k_g is the geometric stiffness matrix, and P_x is the buckling load.

Finally, by adding the stiffness and geometric stiffness matrices, we derive the following finite element equations of the problem:

$$\left(k_1 + k_2 + k_3 - P_x k_g\right) q = 0 \tag{29}$$

The buckling analysis of the shell reverts to the eigenvalue problem, such that

$$\det\left(\left(k_1 + k_2 + k_3\right) - P_x k_g\right) = 0 \tag{30}$$

The following displacement boundary conditions are considered
For clamped supports (CC):

$$v_0, w_0, \varphi_x, \varphi_\theta = 0 \quad at\,(x = 0, \theta),\ (x = \ L,\ \theta) \tag{31}$$

And for simply supports (SS):

$$v_0, w_0 = 0 \quad at\,(x = 0, \theta),\ (x = \ L,\ \theta) \tag{32}$$

4. Numerical Investigation

4.1. Validation

The numerical investigation starts by considering a validation step, where the numerical results are first derived for homogenous stiffened cylindrical panels with rings and stringers and subjected to an axial load and SS boundary conditions, while comparing them to predictions from a commercial code. To this end, in such a preliminary analysis, we assume a null value of weight fraction for GPLs, while considering the following mechanical properties for the matrix: $E_m = 3$ GPa, $\rho_m = 1200\ \mathrm{kg/m^3}$, $\nu_m = 0.34$, $\Delta = 0$ wt % . The geometry of the cylindrical panel is defined by means of $L = 2,\ R = 0.5$, $\beta = 120°$ under the same assumption for the geometrical parameters of rings and stringers: $h_r = h_s = 0.02$, $b_r = b_s = 0.04$, $S_r = 0.5$, $S_s = 0.378$, $N_r = N_s = 5$. (N_r is the number of rings, and N_s is the number of stringers). Table 1 summarizes the results from our formulation in terms of the first six buckling load values, compared to predictions from literature, with a very good accordance among them. This confirms the accuracy of the proposed approach, which enables the subsequent parametric analysis for tunable geometries of stiffeners and mechanical properties of the reinforcement phase. Figure 2 also depicts the corresponding first six buckling mode shapes for the SS-supported stiffened panel, involving different symmetric and asymmetric deformations, according to the selected boundary conditions.

Table 1. Buckling loads (MN/m) as predicted by our formulation and a commercial code.

Buckling Load	λ_1	λ_2	λ_3	λ_4	λ_5	λ_6
Commercial code	10.171	10.19	10.40	10.451	10.910	11.261
Present	10.175	10.20	10.42	10.458	10.977	11.299

In addition, to ensure the correct implementation of equivalent mechanical properties of FG-GPL structures, the critical buckling load of a multilayer FG-GPL cylindrical shell ($\beta = 360°$) under an axial load without stiffeners has been determined and compared with Ref. [53] (Table 2). To this end, we set E_r and $E_s = 0$ in the Matlab Code, and the geometry and mechanical properties are assumed according to Ref. [53]. The governing equations of [53] are based on the classical Donnell shell theory, and the results of the present study are based on FSDT. The comparison between the present results and Ref. [53] for different weight fractions of GPLs and various distributions of nanofillers shows an excellent agreement (Table 2).

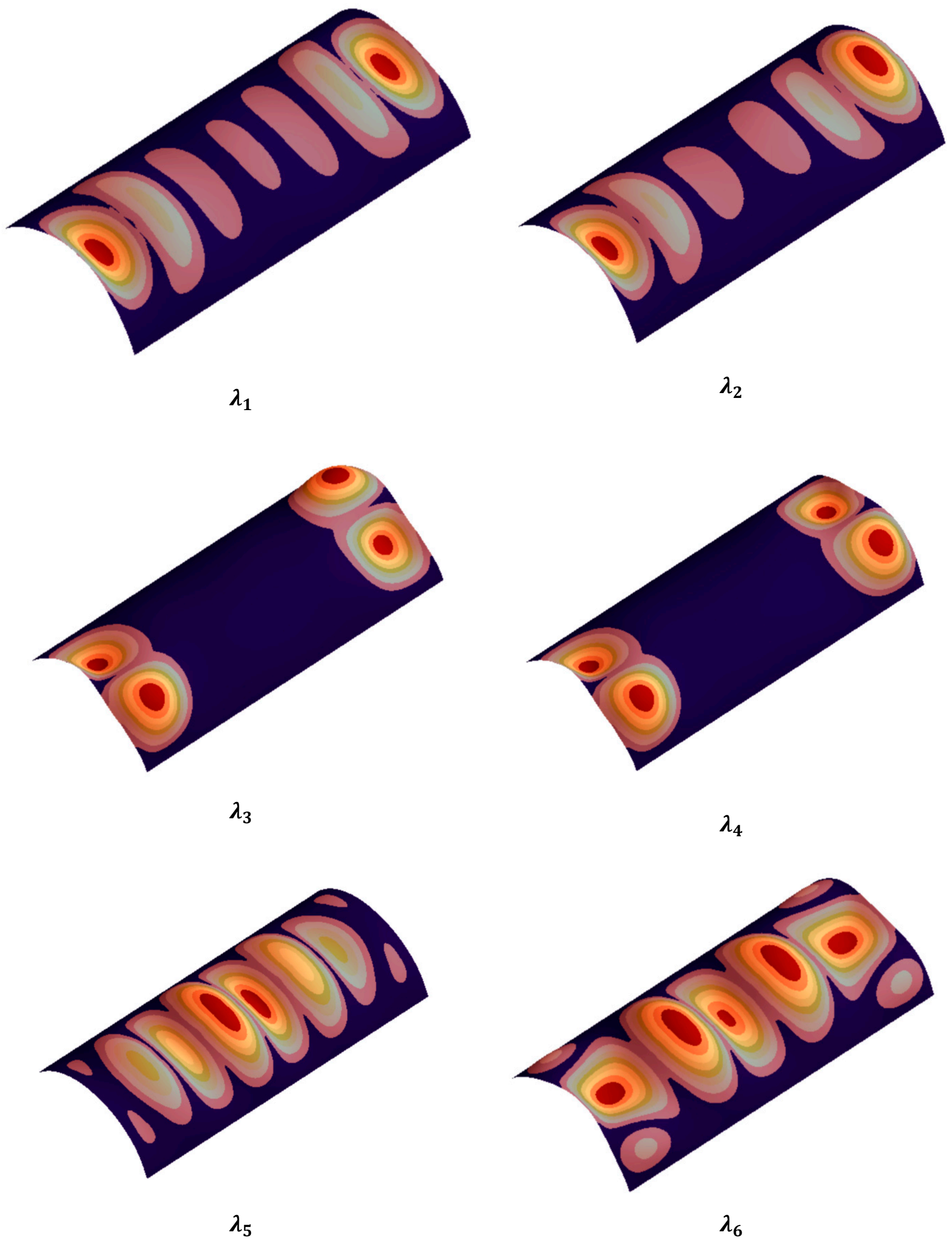

λ_1 λ_2

λ_3 λ_4

λ_5 λ_6

Figure 2. First six buckling mode shapes of a stiffened cylindrical panel (SS boundary condition, $N_r = N_s = 5$, GPLX $\Delta = 0.01$ wt. %).

Table 2. Comparison of critical buckling load of a multilayer FG-GPL cylindrical shell for present study and Ref. [53] ($R = 40h$, $L = 2R$, $h = 0.045$ m).

Δ	**0**	**0.1**	**0.2**	**0.3**	**0.5**	**0.8**	**1**
Present (UD)	21.53	39.19	56.75	74.38	109.40	161.75	196.60
[53] (UD)	21.58	39.22	56.83	74.41	109.48	161.87	196.65
Present (FG-X)	21.53	44.80	67.52	90.15	135.25	202.50	247.21
[53] (FG-X)	21.58	44.82	67.59	90.23	135.30	202.59	247.27
Present (FG-O)	21.53	31.93	41.40	50.35	67.70	92.95	109.53
[53] (FG-O)	21.58	31.99	41.42	50.42	67.76	93.01	109.56

4.2. Numerical Results

4.2.1. Convergence Study

A convergence study is now performed for the first buckling load of stiffened FG-GPL cylindrical shell panels, as summarized in the Table 3. In this case, the critical buckling load of a stiffened multilayer cylindrical panel reinforced by GPLs with simply supported boundary conditions is obtained for a different number of elements (GPL-X, Δ = 1 wt. %, S_s = 0.378, S_r = 0.5). The convergence study is shown in Table 3, where accurate results are obtained by applying 30 and 45 elements in the circumferential and axial directions, respectively.

Table 3. Convergence study of the first buckling load of structure (GPL-X, Δ = 1 wt. %).

Number of Ements ($\mathrm{n_\theta} \times \mathrm{n_x}$)	10 × 15	15 × 25	20 × 30	25 × 35	30 × 45
Buckling load	70.02	66.18	60.12	55.22	54.69

4.2.2. Numerical Results of Present Investigation

The numerical analysis continues by evaluating the first six buckling loads for a stiffened multilayer cylindrical panel reinforced by GPLs, accounting for the sensitivity of the axial buckling response to different reinforcement patterns and weight fractions, but also to different boundary conditions and numbers of rings and stringers. In this case, the stiffened FG-GPL multilayer cylindrical panel assumes the following mechanical properties: $E_m = 3$ GPa ,$\nu_m = 0.34$, $\rho_m = 1200\ \mathrm{kg/m^3}$ (for the matrix phase), and $E_{GPL} = 1.01$ TPa, $\nu_{GPL} = 0.186$, $\rho_{GPL} = 1062.5\ \mathrm{kg/m^3}$, $w_{GPL} = 1.5\ \mu\mathrm{m}$, $l_{GPL} = 2.5\ \mu\mathrm{m}$, $t_{GPL} = 1.5$ nm (for the reinforcement phase). The same geometrical properties assumed before are considered once again in this case for the cylindrical panel with stiffeners.

Table 4 summarizes the effect of different GPL patterns on the buckling load of the shell, for a SS boundary condition, under the assumption of a weight fraction Δ = 1 wt. %. Based on this table, the GPLX pattern seems to yield the highest buckling loads of the structure compared to other GPL patterns, whereas the GPLO pattern seems to obtain the lowest buckling loads. Such differences are approximately estimated equal to 40% as acceptable for design purposes among engineers. At the same time, when the concentration of the nanofiller phase at the external sides of the panel is higher than the concentration in the core, the structure increases its mechanical stiffness. Table 4 also describes the impact of GPL weight fractions on the buckling load of the structure. More specifically, by enhancing the weight fraction of nanofillers from 0 to 0.01, for different GPL patterns, the buckling load increases significantly (approximately 400% for a GPL-X pattern). The impact of an increased weight fraction of GPLs on the buckling load of the structure is more pronounced for a GPL-X distribution than other patterns, and the impact of an increased weight fraction of nanofillers on the buckling load for GPL-O is less pronounced than the other patterns. In Table 5, we also show the sensitivity of the buckling response to varying boundary conditions, under the same assumptions for S_r, S_s, N_r, N_s, Δ. As visible from this table, a CC boundary condition yields higher buckling loads than a SS boundary condition, due to the increased stiffness of a CC boundary condition versus a SS structure, with a relative difference of about 15%. Table 6 also shows the influence of the number of stiffeners (rings and stringers) on the buckling load of the stiffened cylindrical panel for both boundary conditions, under the assumption of uniform distribution for GPLs (GPL-UD) and a weight fraction of nanofillers Δ = 1 wt. %. Based on results, it is worth noticing that an increased number of rings and stringers, from five to ten, provides an increased buckling load of about 15% for both boundary conditions. The first six buckling mode shapes of the shell panel are represented in Figures 2 and 3 for a SS and CC boundary condition, respectively, while keeping the same number of ribs and stringers, $N_r = N_s = 5$, whereas the last two figures (Figures 4 and 5) show the corresponding mode shapes for an increased number of stiffeners, $N_r = N_s = 10$, with a clearly different deformed configuration just related to the varied number of stiffeners, under the same boundary condition. More in detail, based on a comparative evaluation of Figure 2 with Figures 3 and 4 with Figure 5, an increased number of stiffeners clearly reduces the overall deformability of the structure, as highlighted in all symmetric and asymmetric deformed configurations, for each mode shape.

Table 4. Effect of GPL weight fractions on the buckling load (MN/m) of a SS structure (S_s = 0.378, S_r = 0.5).

GPL Pattern	Δ_{GPL} %	λ_1	λ_2	λ_3	λ_4	λ_5	λ_6
GPL-X	0	10.175	10.20	10.42	10.458	10.977	11.299
	0.5	31.222	31.270	32.086	32.096	35.129	35.176
	1	54.699	54.776	56.103	56.119	59.421	61.046
GPL-A	0	10.175	10.20	10.42	10.458	10.977	11.299
	0.5	25.318	25.348	25.876	25.882	27.194	27.999
	1	41.118	41.168	42.025	42.035	44.166	45.474
GPL-UD	0	10.175	10.20	10.42	10.458	10.977	11.299
	0.5	27.050	27.083	27.646	27.653	29.055	29.915
	1	43.931	43.984	44.899	44.910	47.187	48.584
GPL-O	0	10.175	10.20	10.42	10.458	10.977	11.299
	0.5	24.345	24.374	24.881	24.887	26.149	26.923
	1	39.537	39.585	40.409	40.419	42.468	43.725

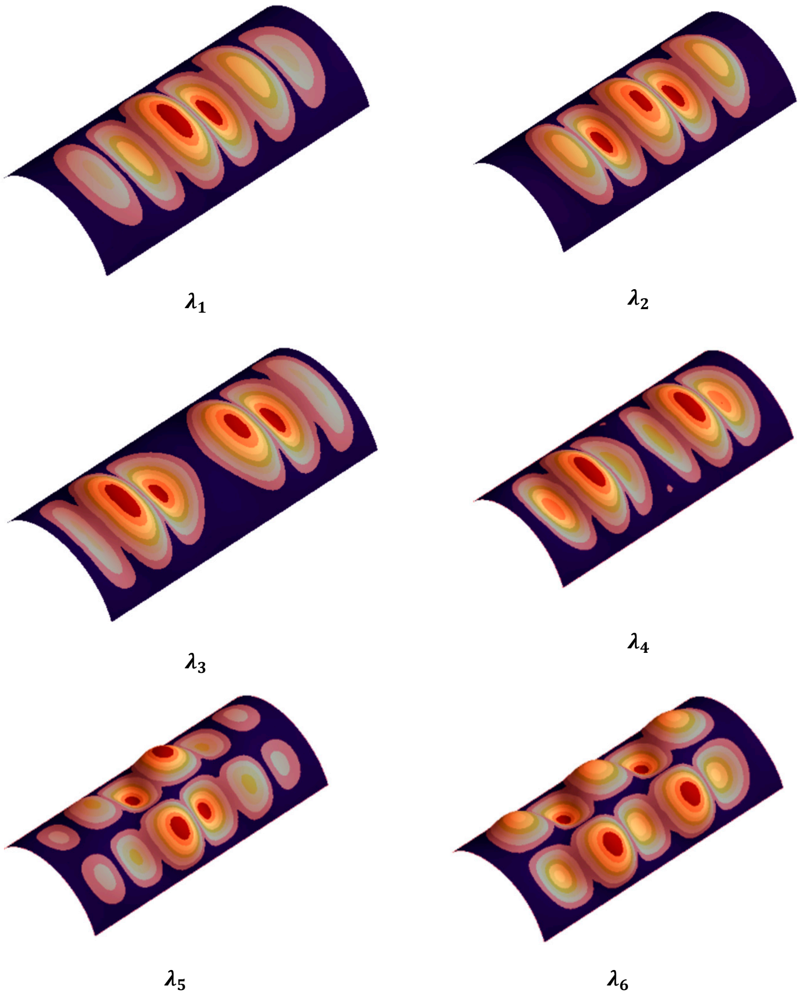

λ_1 λ_2

λ_3 λ_4

λ_5 λ_6

Figure 3. First six buckling mode shapes of a stiffened cylindrical panel (CC boundary condition, $N_r = N_s = 5$, GPLX Δ = 0.01 wt. %).

Table 5. Effect of boundary conditions on the buckling load (MN/m) for SS and CC structures (S_s = 0.378, S_r = 0.5, Δ = 1 wt. %).

GPL Pattern	Boundary Condition	λ_1	λ_2	λ_3	λ_4	λ_5	λ_6
GPL-X	CC	61.625	61.698	64.257	64.266	68.720	71.201
	SS	54.699	54.776	56.103	56.119	59.421	61.046
GPL-UD	CC	47.120	47.789	51.749	51.798	53.942	53.980
	SS	43.931	43.984	44.899	44.910	47.187	48.584
GPL-O	CC	45.102	45.121	46.201	46.211	48.070	49.924
	SS	39.537	39.585	40.409	40.419	42.468	43.725
GPL-A	CC	46.505	46.521	47.782	47.788	49.225	51.025
	SS	41.118	41.168	42.025	42.035	44.166	45.474

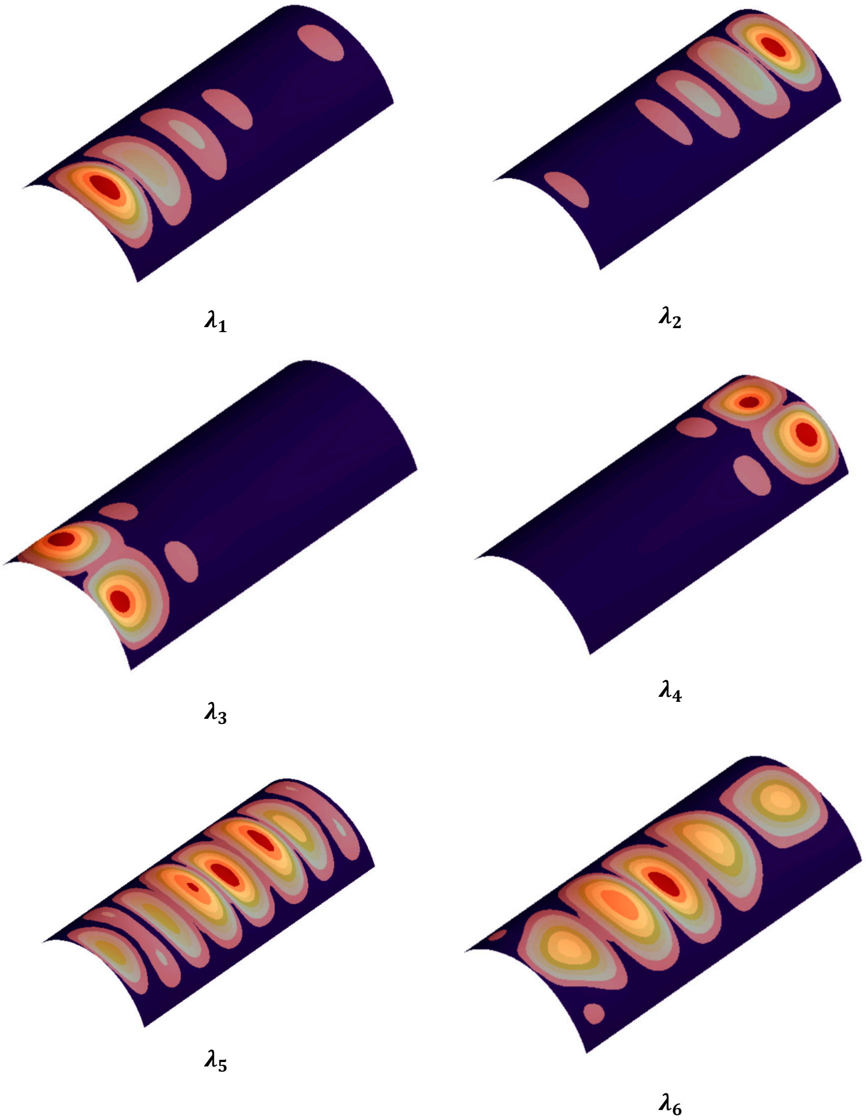

λ_1 λ_2

λ_3 λ_4

λ_5 λ_6

Figure 4. First six buckling mode shapes of a stiffened cylindrical panel (SS boundary condition, $N_r = N_s = 10$, GPLX Δ = 0.01 wt. %).

Table 6. Impact of the number of rings and stringers on the buckling loads (MN/m) of the structure (GPL-UD, Δ = 1 wt. %).

Boundary Condition	**Number of Rings and Stringers**	λ_1	λ_2	λ_3	λ_4	λ_5	λ
CC	$S_s = 0.378$, $S_r = 0.5$ or $N_r = N_s = 5$	47.120	47.789	51.749	51.798	53.942	53.980
	$S_s = 0.19$, $S_r = 0.25$ or $N_r = N_s = 10$	52.953	53.194	57.373	59.296	60.925	60.996
SS	$S_s = 0.378$, $S_r = 0.5$ or $N_r = N_s = 5$	43.931	43.984	44.899	44.910	47.187	48.584
	$S_s = 0.19$, $S_r = 0.25$ or $N_r = N_s = 10$	49.112	49.799	51.473	52.307	53.725	53.908

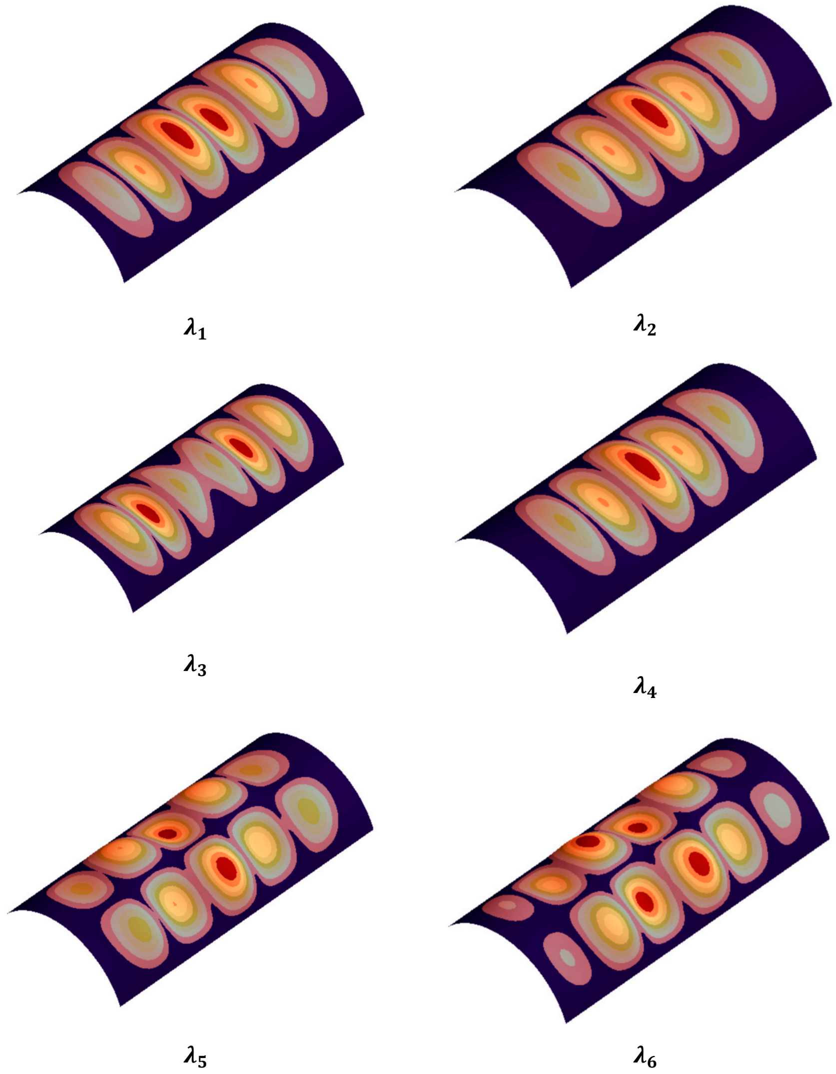

Figure 5. First six buckling mode shapes of a stiffened cylindrical panel (CC boundary condition, $N_r = N_s = 10$, GPLX Δ = 0.01 wt. %).

5. Conclusions

This work has focused on the buckling response of stiffened cylindrical panels reinforced with GPLs subjected to an axial loading. Four different patterns of GPLs, including GPL-X, GPL-O, GPL UD, and GPL-A, have been considered here across the shell thickness. The first-order shear deformation theory and finite element approach have permitted us to define and approximately solve the governing equations of the problem. A systematic investigation has been performed to assess the sensitivity of the response to different GPL patterns and weight fractions, but also to different boundary conditions and numbers of stringers and rings. The final remarks can be summarized as follows:

(a) The maximum and minimum values of the buckling load stem from a GPL-X and GPL-O distribution, respectively.
(b) The maximum variation in the buckling load for different GPL patterns and weight fractions is approximately equal to 40% and 400%, respectively.
(c) The buckling load of the structure tends to increase for increased reinforcement weight fractions, especially for a GPL-X pattern, compared to other GPL distributions.
(d) A CC boundary condition provides higher buckling loads (of approximately 15%) compared to the results from a SS boundary condition.
(e) The buckling load can be increased by about 15% for each fixed boundary condition, for an increased number of rings and stringers from five to ten.

Our parametric results could be a valid reference for structural design optimization purposes, due to the capability of FG GPLs to change the stiffness and strength properties of the composite panels with different boundary conditions, by simply tuning the geometry of the stiffeners, as well as the reinforcement distribution and weight fraction.

Author Contributions: Conceptualization, F.T. and R.D.; Methodology, Z.L., F.T., R.D. and M.B.; Validation, Z.L., F.T., R.D. and M.B.; Formal analysis, Z.L. and M.B.; Investigation, F.T., R.D. and M.B.; Writing—original draft, Z.L. and M.B.; Writing—review & editing, F.T. and R.D.; Visualization, Z.L.; Supervision, F.T. and R.D. All authors have read and agreed to the published version of the manuscript.

Funding: This research received no external funding.

Data Availability Statement: Data are contained within the article.

Conflicts of Interest: The authors declare no conflict of interest.

References

1. Mollaei, S.; Babaei, M.; Asemi, K. Torsional buckling of functionally graded graphene reinforced composite laminated cylindrical panel. *Arch. Appl. Mech.* **2023**, *93*, 427–435. [CrossRef]
2. Kiani, Y. Buckling of functionally graded graphene reinforced conical shells under external pressure in thermal environment. *Compos. Part B Eng.* **2019**, *156*, 128–137. [CrossRef]
3. Lei, Z.; Su, Q.; Zeng, H.; Zhang, Y.; Yu, C. Parametric studies on buckling behavior of functionally graded graphene-reinforced composites laminated plates in thermal environment. *Compos. Struct.* **2018**, *202*, 695–709. [CrossRef]
4. Shahgholian-Ghahfarokhi, D.; Safarpour, M.; Rahimi, A. Torsional buckling analyses of functionally graded porous nanocomposite cylindrical shells reinforced with graphene platelets (GPLs). *Mech. Based Des. Struct. Mach.* **2021**, *49*, 81–102. [CrossRef]
5. Shahgholian-Ghahfarokhi, D.; Rahimi, G.; Khodadadi, A.; Salehipour, H.; Afrand, M. Buckling analyses of FG porous nanocomposite cylindrical shells with graphene platelet reinforcement subjected to uniform external lateral pressure. *Mech. Based Des. Struct. Mach.* **2021**, *49*, 1059–1079. [CrossRef]
6. Dong, Y.H.; He, L.W.; Wang, L.; Li, Y.H.; Yang, J. Buckling of spinning functionally graded graphene reinforced porous nanocomposite cylindrical shells: An analytical study. *Aerosp. Sci. Technol.* **2018**, *82*, 466–478. [CrossRef]
7. Chen, D.; Yang, J.; Kitipornchai, S. Nonlinear vibration and postbuckling of functionally graded graphene reinforced porous nanocomposite beams. *Compos. Sci. Technol.* **2017**, *142*, 235–245. [CrossRef]
8. Kitipornchai, S.; Chen, D.; Yang, J. Free vibration and elastic buckling of functionally graded porous beams reinforced by graphene platelets. *Mater. Des.* **2017**, *116*, 656–665. [CrossRef]
9. Zhang, W.; Wang, C.; Wang, Y. Thermo-mechanical analysis of porous functionally graded graphene reinforced cylindrical panels using an improved third order shear deformable model. *Appl. Math. Model.* **2023**, *118*, 453–473. [CrossRef]
10. Sobhani, E.; Arbabian, A.; Civalek, Ö.; Avcar, M. The free vibration analysis of hybrid porous nanocomposite joined hemispherical–cylindrical–conical shells. *Eng. Comput.* **2021**, *38*, 3125–3152.
11. Yang, J.; Chen, D.; Kitipornchai, S. Buckling and free vibration analyses of functionally graded graphene reinforced porous nanocomposite plates based on Chebyshev-Ritz method. *Compos. Struct.* **2018**, *193*, 281–294. [CrossRef]
12. Zhou, Z.; Ni, Y.; Tong, Z.; Zhu, S.; Sun, J.; Xu, X. Accurate nonlinear buckling analysis of functionally graded porous graphene platelet reinforced composite cylindrical shells. *Int. J. Mech. Sci.* **2019**, *151*, 537–550. [CrossRef]
13. Ansari, R.; Hassani, R.; Gholami, R.; Rouhi, H. Buckling and Postbuckling of Plates Made of FG-GPL-Reinforced Porous Nanocomposite with Various Shapes and Boundary Conditions. *Int. J. Struct. Stab. Dyn.* **2021**, *21*, 2150063. [CrossRef]

14. Yaghoobi, H.; Taheri, F. Analytical solution and statistical analysis of buckling capacity of sandwich plates with uniform and non-uniform porous core reinforced with graphene nanoplatelets. *Compos. Struct.* **2020**, *252*, 112700. [CrossRef]
15. Tao, C.; Dai, T. Isogeometric analysis for postbuckling of sandwich cylindrical shell panels with graphene platelet reinforced functionally graded porous core. *Compos. Struct.* **2021**, *260*, 113258. [CrossRef]
16. Nguyen, Q.H.; Nguyen, L.B.; Nguyen, H.B.; Nguyen-Xuan, H. A three-variable high order shear deformation theory for isogeometric free vibration, buckling and instability analysis of FG porous plates reinforced by graphene platelets. *Compos. Struct.* **2020**, *245*, 112321. [CrossRef]
17. Priyanka, R.; Twinkle, C.M.; Pitchaimani, J. Stability and dynamic behavior of porous FGM beam: Influence of graded porosity, graphene platelets, and axially varying loads. *Eng. Comput.* **2021**, *38*, 4347–4366. [CrossRef]
18. Barati, M.R.; Zenkour, A.M. Analysis of postbuckling of graded porous GPL-reinforced beams with geometrical imperfection. *Mech. Adv. Mater. Struct.* **2019**, *26*, 503–511. [CrossRef]
19. Anirudh, B.; Ganapathi, M.; Anant, C.; Polit, O. A comprehensive analysis of porous graphene-reinforced curved beams by finite element approach using higher-order structural theory: Bending, vibration and buckling. *Compos. Struct.* **2019**, *222*, 110899. [CrossRef]
20. Li, Z.; Zheng, J. Nonlinear stability of the encased functionally graded porous cylinders reinforced by graphene nanofillers subjected to pressure loading under thermal effect. *Compos. Struct.* **2020**, *233*, 111584. [CrossRef]
21. Twinkle, C.M.; Pitchaimani, J. Free vibration and stability of graphene platelet reinforced porous nano-composite cylindrical panel: Influence of grading, porosity and non-uniform edge loads. *Eng. Struct.* **2021**, *230*, 111670.
22. Tornabene, F.; Viscoti, M.; Dimitri, R. Higher order theories for the modal analysis of anisotropic doubly-curved shells with a three-dimensional variation of the material properties. *Eng. Anal. Bound. Elem.* **2024**, *158*, 486–519. [CrossRef]
23. Wang, Z.W.; Tang, J.; Li, S.C.; He, X.H.; Zhou, C.Y. Research on Elastic and Elastics-Plastic Buckling Load of Cylindrical Shell with an Inclined through Crack under Axial Compressive Load. *Materials* **2023**, *16*, 6123. [CrossRef] [PubMed]
24. Yas, M.H.; Rahimi, S. Thermal buckling analysis of porous functionally graded nanocomposite beams reinforced by graphene platelets using Generalized differential quadrature method. *Aerosp. Sci. Technol.* **2020**, *107*, 106261. [CrossRef]
25. Gao, K.; Do, D.M.; Li, R.; Kitipornchai, S.; Yang, J. Probabilistic stability analysis of functionally graded graphene reinforced porous beams. *Aerosp. Sci. Technol.* **2020**, *98*, 105738. [CrossRef]
26. Alimoradzadeh, M.; Tornabene, F.; Dimitri, R. Nonlinear axial-lateral coupled vibration of functionally graded-fiber reinforced composite laminated (FG-FRCL) beams subjected to aero-thermal loads. *Int. J. Non-Linear Mech.* **2024**, *159*, 104612. [CrossRef]
27. Salmani, R.; Gholami, R.; Ansari, R.; Fakhraie, M. Analytical investigation on the nonlinear postbuckling of functionally graded porous cylindrical shells reinforced with graphene nanoplatelets. *Eur. Phys. J. Plus* **2021**, *136*, 53. [CrossRef]
28. Li, Z.; Zhang, Q.; Shen, H.; Xiao, X.; Kuai, H.; Zheng, J. Buckling performance of the encased functionally graded porous composite liner with polyhedral shapes reinforced by graphene platelets under external pressure. *Thin-Walled Struct.* **2023**, *183*, 110370. [CrossRef]
29. Shahani, A.R.; Kiarasi, F. Numerical and Experimental Investigation on Post-buckling Behavior of Stiffened Cylindrical Shells with Cutout subject to Uniform Axial Compression. *J. Appl. Comput. Mech.* **2023**, *9*, 25–44.
30. Wu, Q.; Hu, S.; Tang, X.; Liu, X.; Chen, Z.; Xiong, J. Compressive buckling and post-buckling behaviors of J-type composite stiffened panel before and after impact load. *Compos. Struct.* **2023**, *304*, 116339. [CrossRef]
31. Tran, K.L.; Douthe, C.; Sab, K.; Dallot, J.; Davaine, L. Buckling of stiffened curved panels under uniform axial compression. *J. Constr. Steel Res.* **2014**, *103*, 140–147. [CrossRef]
32. Grondin, G.Y.; Elwi, A.E.; Cheng, J.J.R. Buckling of stiffened steel plates—A parametric study. *J. Constr. Steel Res.* **1999**, *50*, 151–175. [CrossRef]
33. Reddy, J.N.; Starnes, J.H., Jr. General buckling of stiffened circular cylindrical shells according to a layerwise theory. *Comput. Struct.* **1993**, *49*, 605–616. [CrossRef]
34. Ni, X.Y.; Prusty, B.G.; Hellier, A.K. Buckling and post-buckling of isotropic and composite stiffened panels: A review on optimisation (2000–2015). *Int. J. Marit. Eng.* **2016**, *158*, A-251–A-267. [CrossRef]
35. Wodesenbet, E.; Kidane, S.; Pang, S.S. Optimization for buckling loads of grid stiffened composite panels. *Compos. Struct.* **2003**, *60*, 159–169. [CrossRef]
36. Ni, X.Y.; Prusty, B.G.; Hellier, A.K. Buckling and post-buckling of isotropic and composite stiffened panels: A review on analysis and experiment (2000–2012). *Int. J. Marit. Eng.* **2015**, *157*. [CrossRef]
37. Kidane, S.; Li, G.; Helms, J.; Pang, S.S.; Woldesenbet, E. Buckling load analysis of grid stiffened composite cylinders. *Compos. Part B Eng.* **2003**, *34*, 1–9. [CrossRef]
38. Wang, D.; Abdalla, M.M.; Zhang, W. Buckling optimization design of curved stiffeners for grid-stiffened composite structures. *Compos. Struct.* **2017**, *159*, 656–666. [CrossRef]
39. Patel, S.N.; Datta, P.K.; Sheikh, A.H. Buckling and dynamic instability analysis of stiffened shell panels. *Thin-Walled Struct.* **2006**, *44*, 321–333. [CrossRef]
40. Ifayefunmi, O.; Ruan, D. Buckling of Stiffened Cone–Cylinder Structures Under Axial Compression. *Int. J. Appl. Mech.* **2022**, *14*, 2250075. [CrossRef]
41. Zarei, M.; Rahimi, G.H.; Hemmatnezhad, M. On the buckling resistance of grid-stiffened composite conical shells under compression. *Eng. Struct.* **2021**, *237*, 112213. [CrossRef]

42. Yoon, J.W.; Bray, G.H.; Valente RA, F.; Childs, T.E.R. Buckling analysis for an integrally stiffened panel structure with a friction stir weld. *Thin-Walled Struct.* **2009**, *47*, 1608–1622. [CrossRef]
43. Duc, N.D.; Thang, P.T. Nonlinear buckling of imperfect eccentrically stiffened metal–ceramic–metal S-FGM thin circular cylindrical shells with temperature-dependent properties in thermal environments. *Int. J. Mech. Sci.* **2014**, *81*, 17–25. [CrossRef]
44. Duc, N.D.; Thang, P.T. Nonlinear response of imperfect eccentrically stiffened ceramic–metal–ceramic FGM thin circular cylindrical shells surrounded on elastic foundations and subjected to axial compression. *Compos. Struct.* **2014**, *110*, 200–206. [CrossRef]
45. Duc, N.D. Nonlinear dynamic response of imperfect eccentrically stiffened FGM double curved shallow shells on elastic foundation. *Compos. Struct.* **2013**, *99*, 88–96. [CrossRef]
46. Duc, N.D.; Cong, P.H. Nonlinear thermal stability of eccentrically stiffened functionally graded truncated conical shells surrounded on elastic foundations. *Eur. J. Mech.-A/Solids* **2015**, *50*, 120–131. [CrossRef]
47. Wang, Y.; Xie, K.; Fu, T.; Shi, C. Bending and elastic vibration of a novel functionally graded polymer nanocomposite beam reinforced by graphene nanoplatelets. *Nanomaterials* **2019**, *9*, 1690. [CrossRef] [PubMed]
48. Liu, D. Free vibration of functionally graded graphene platelets reinforced magnetic nanocomposite beams resting on elastic foundation. *Nanomaterials* **2020**, *10*, 2193. [CrossRef] [PubMed]
49. Zhang, J.; Lv, Y.; Li, L. Dynamic Instability of Functionally Graded Graphene Platelet-Reinforced Porous Beams on an Elastic Foundation in a Thermal Environment. *Nanomaterials* **2022**, *12*, 4098. [CrossRef]
50. Babaei, M.; Kiarasi, F.; Asemi, K.; Dimitri, R.; Tornabene, F. Transient Thermal Stresses in FG Porous Rotating Truncated Cones Reinforced by Graphene Platelets. *Appl. Sci.* **2022**, *12*, 3932. [CrossRef]
51. Zhou, Z.; Wang, Y.; Zhang, S.; Dimitri, R.; Tornabene, F.; Asemi, K. Numerical Study on the Buckling Behavior of FG Porous Spherical Caps Reinforced by Graphene Platelets. *Nanomaterials* **2023**, *13*, 1205. [CrossRef] [PubMed]
52. Dong, D.T.; Van Dung, D. A third-order shear deformation theory for nonlinear vibration analysis of stiffened functionally graded material sandwich doubly curved shallow shells with four material models. *J. Sandw. Struct. Mater.* **2019**, *21*, 1316–1356. [CrossRef]
53. Blooriyan, S.; Ansari, R.; Darvizeh, A.; Gholami, R.; Rouhi, H. Postbuckling analysis of functionally graded graphene platelet-reinforced polymer composite cylindrical shells using an analytical solution approach. *Appl. Math. Mech.* **2019**, *40*, 1001–1016. [CrossRef]